Robust Short-Lag Spatial Coherence Imaging

Arun Asokan Nair[1], *Student Member, IEEE,* Trac Duy Tran[1], *Fellow, IEEE,*
and Muyinatu A. Lediju Bell[1,2], *Member, IEEE*

***Abstract*—Short-lag spatial coherence (SLSC) imaging displays the spatial coherence between backscattered ultrasound echoes instead of their signal amplitudes and is more robust to noise and clutter artifacts when compared to traditional delay-and-sum (DAS) B-mode imaging. However, SLSC imaging does not consider the content of images formed with different lags, and thus does not exploit the differences in tissue texture at each short lag value. Our proposed method improves SLSC imaging by weighting the addition of lag values (i.e., M-weighting) and by applying Robust Principal Component Analysis (RPCA) to search for a low dimensional subspace for projecting coherence images created with different lag values. The RPCA-based projections are considered to be de-noised versions of the originals that are then weighted and added across lags to yield a final Robust Short-Lag Spatial Coherence (R-SLSC) image. Our approach was tested on simulation, phantom, and *in vivo* liver data. Relative to DAS B-mode images, the mean contrast, signal-to-noise ratio (SNR), and contrast-to-noise ratio (CNR) improvements with R-SLSC images are 21.22 dB, 2.54 and 2.36 respectively, when averaged over simulated, phantom, and *in vivo* data and over all lags considered which corresponds to mean improvements of 96.4%, 121.2% and 120.5% respectively. When compared to SLSC images, the corresponding mean improvements with R-SLSC images were 7.38 dB, 1.52 and 1.30, respectively, (i.e., mean improvements of 14.5%, 50.5% and 43.2%, respectively). Results show great promise for smoothing out the tissue texture of SLSC images and enhancing anechoic or hypoechoic target visibility at higher lag values which could be useful in clinical tasks such as breast cyst visualization, liver vessel tracking, and obese patient imaging.**

I. Introduction

DISPLAYING the spatial coherence of backscattered ultrasound waves is a promising alternative to generate ultrasound image contrast when compared to traditional, amplitude-based delay-and-sum (DAS) beamforming. This alternative is motivated by the van Cittert Zernike (VCZ) theorem applied to ultrasound[1], [2], [3], which states that for an incoherent source and a spatially incoherent medium, the expected spatial coherence is the squared Fourier transform of the product of the transmit beam intensity distribution and the reflectivity profile of the insonified medium.

The VCZ theorem supported ultrasound-based investigations by Mallart and Fink[4], Liu and Waag[5], and Bamber et al.[6], and led to the development of short-lag spatial coherence (SLSC)[7] imaging. SLSC imaging has since demonstrated remarkable improvements over traditional ultrasound B-mode imaging when visualizing liver tissue[8], endocardial borders[9], fetal anatomical features[10], and point-like targets in the presence of noise[11]. A suite of traditional ultrasound transducer arrays (i.e., linear[7], curvilinear[8], phased[9], and 2D matrix[12], [13] arrays) were demonstrated to be compatible with SLSC imaging. This new imaging method was additionally extended to photoacoustic imaging to improve the visibility of prostate brachytherapy seeds[14], to improve signal contrast when imaging with low-energy, pulsed laser diodes[15] and to potentially guide minimally invasive surgeries [16]. Additional work in this area has weighted SLSC images with traditional DAS images [17] and utilized SLSC beamforming to reduce clutter and sidelobes in photoacoustic images [18].

SLSC imaging is implemented by computing the spatial correlation between received signals at various element separations (or lags), then summing across the lags to generate the final output image. In doing so, SLSC imaging inherently weights all lags equally and does not consider differences in tissue texture appearances when SLSC images are formed with various combinations of lag values. One possibility to consider texture differences is to apply uneven weighting to the lag images prior to summation. Another possibility is to apply linear dimensionality reduction.

Principal component analysis (PCA)[19] is a popular method for linear dimensionality reduction, with wide-ranging domains of application that include data mining [20], neuroscience[21], and linear control systems[22]. PCA finds the orthogonal directions of highest variance by taking the singular value decomposition of a data matrix and preserving the subspace corresponding to the largest singular values. Assuming that data is corrupted by dense, low-magnitude, Gaussian noise, PCA returns the maximum likelihood estimate for an underlying subspace[23]. Projecting data onto this low-dimensional, underlying subspace, then re-projecting to a high dimensional space is generally a useful denoising technique that eliminates spurious directions of variance corresponding to noise in the data.

PCA was successfully applied to various ultrasound imaging tasks, including motion estimation (by leveraging its signal separation capabilities to reject decorrelation and noise) [24] and on-line classification of arterial stenosis intensity[25]. However, one limitation of PCA is that it lacks robustness[26] and displays a high sensitivity to outliers.

Robust Principal Component Analysis(RPCA)[26], [28], [29] was developed to recover a low rank matrix from a matrix of corrupted observations, particularly when the errors are arbitrarily large. In addition, as stated in[26], in most cases the low rank matrix can be recovered from most common corruptions by solving a convex optimization problem. In

This work is partially supported by the NSF under Grants ECCS-1443936 and CCF-1422995 and by the NIH under Grant R00 EB018994.

The authors are with the [1]Department of Electrical and Computer Engineering and the [2]Department of Biomedical Engineering, Johns Hopkins University, Baltimore, MD (e-mail: anair8@jhu.edu).

the context of ultrasound imaging, RPCA was utilized to automatically classify acoustic radiation force impulse (ARFI) displacement profiles in the presence of high variance outlier profiles[30] and to implement motion-based clutter reduction [31].

In this paper, we propose a modification to the SLSC algorithm to explicitly consider the content of coherence images formed with different lags by applying RPCA to first search for a low dimensional subspace, then project individual coherence images onto this low dimensional subspace. We assume that this approach enables us to denoise the observations at higher lags and incorporate them in our imaging pipeline. The projections are denoised versions of the originals that are then weighted and summed across the lags to yield the final Robust Short-Lag Spatial Coherence (R-SLSC) image. We also consider the effect of weighting without applying RPCA.

Our paper is organized as follows: Section II details the background that motivated this work, specifically the SLSC algorithm and the RPCA algorithm. Section III describes our proposed R-SLSC method in detail. Section IV provides details about our simulation, phantom and experimental data and related evaluation metrics. Section V presents the results of our study, while section VI discusses the strengths and limitations of the proposed algorithm. We conclude our paper in section VII.

II. Background

A. Short-Lag Spatial Coherence (SLSC) Imaging

SLSC beamforming (as discussed extensively in [7], [11], [33]) computes and displays the spatial coherence between backscattered ultrasound echoes at different short lag values, and thereby removes clutter artifacts. The ultrasound channel data consists of echoes received by N equi-spaced detector elements of an array. Assuming s_i is the time-delayed, zero mean data received by the i^{th} detector element, let a measurement corresponding to the n^{th} depth (in samples) of this data be the signal $s_i(n)$. The spatial covariance across the face of the aperture is evaluated as:

$$\hat{C}(m) = \frac{1}{N-m} \sum_{i=1}^{N-m} \sum_{n=n_1}^{n_2} s_i(n) s_{i+m}(n) \tag{1}$$

where m is the lag (in number of elements) between two detector elements of the array. The size of the correlation kernel (i.e., $n_2 - n_1$) is fixed to be approximately one wavelength in order to maintain an axial resolution similar to that of DAS B-mode images without compromising the stability of the calculated coherence functions.

Eq. (1) is normalized by the individual variances of the two scan lines being considered, and the spatial correlation $\hat{R}$ at lag m is:

$$\hat{R}(m) = \frac{1}{N-m} \sum_{i=1}^{N-m} \frac{\sum_{n=n_1}^{n_2} s_i(n) s_{i+m}(n)}{\sqrt{\sum_{n=n_1}^{n_2} s_i^2(n) \sum_{n=n_1}^{n_2} s_{i+m}^2(n)}} \tag{2}$$

which results in a spatial coherence function. We integrate this spatial coherence function over the first M lags to achieve a SLSC image pixel:

$$R_{sl} = \int_{m=1}^{M} \hat{R}(m) dm \approx \sum_{m=1}^{M} \hat{R}(m) \tag{3}$$

Eqs. (1)-(3) are repeated at various axial and lateral positions to generate a SLSC image.

The coherence functions scale with the size of the aperture, thus M is expressed in terms of a quantity Q, which is defined to be the percentage fraction of the receive aperture over which we are summing, i.e.:

$$Q = \frac{M}{N} \times 100\% \tag{4}$$

in order to standardize across various receive aperture sizes.

B. Robust Principal Component Analysis (RPCA)

RPCA[26], [28] is implemented by finding a low-rank approximation A of a noisy observation matrix D, which can be expressed as:

$$D = A + E + N \tag{5}$$

where A is the low-rank ground truth matrix, E is an error matrix which is considered to be sparse but allowed to have high magnitude errors, while N contains dense, low-magnitude errors. The main objective is to calculate the lowest rank A that approximates the data subject to the outlier errors being sparse i.e. $\|E\|_0 \leq K$ for some appropriately chosen threshold K (where $\|.\|_0$ is the L_0 norm, which counts the number of non-zero entries in E). Writing out the Lagrangian formulation, we obtain:

$$\min_{A,E} \text{Rank}(A) + \lambda \|E\|_0 \text{ subject to } D = A + E + N \approx A + E \tag{6}$$

where λ is a penalty factor based on the quantity of outliers present in data. Note that Eq. (6) is difficult to optimize as it is non-convex. Relaxing the rank constraint to a nuclear norm constraint and the L_0 norm constraint to an L_1 norm constraint, we rewrite Eq. (6) as:

$$\min_{A,E} \|A\|_* + \lambda \|E\|_1 \text{ subject to } D \approx A + E \tag{7}$$

where the nuclear norm, $\|.\|_*$, is the sum of the singular values of a matrix. This relaxation is reasonable because the solution to (7) is almost always the same as the solution to (6), as proved in [26].

To solve Eq. (7), we utilized a numerical optimization method based on the Augmented Lagrangian Multiplier (ALM) [28] method. This solver relaxes Eq. (7) by solving for the minimum of the Lagrangian $L(A, E, Y, \mu)$ of the problem, where $L(A, E, Y, \mu)$ is defined as:

$$L(A, E, Y, \mu) = \|A\|_* + \lambda \|E\|_1 + \langle Y, D - A - E \rangle + \frac{\mu}{2} \|D - A - E\|_F^2$$

We used the MATLAB inexact ALM solver based on[28] and hosted at[32] to perform RPCA.

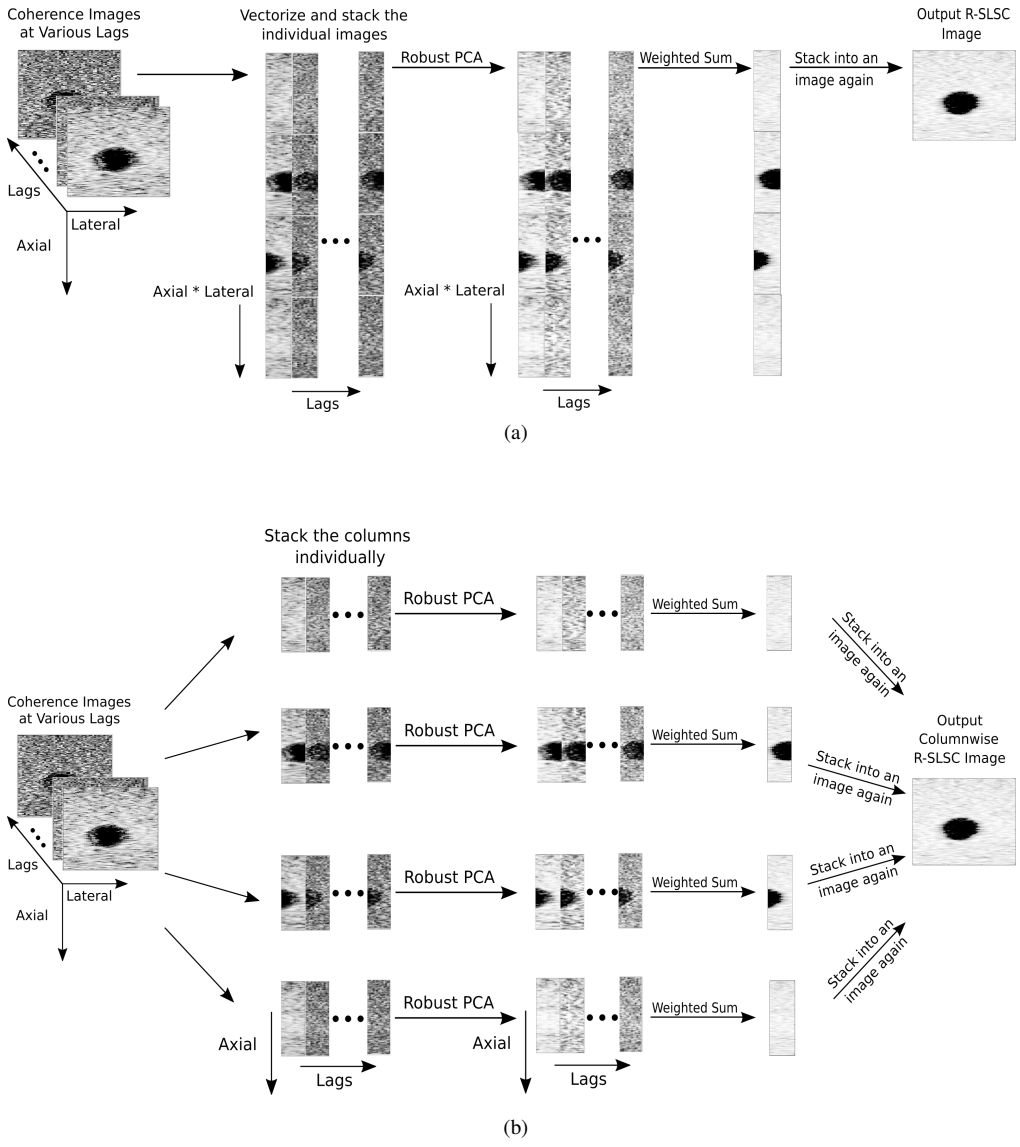

Fig. 1: (a) Summary of the the whole-image R-SLSC imaging process. The individual coherence images up to a specific lag M are vectorized and stacked into a matrix. RPCA is performed on this data matrix, and the denoised coherence images are weighted and summed across the lag dimension. Finally, the vectorization is reversed to yield the output R-SLSC image at lag M. (b) Columnwise R-SLSC imaging is similar, with the exception that the whole image is subdivided into individual columns for the denoising step. Patchwise R-SLSC imaging (not shown) denoises individual patches rather than columns.

III. Proposed Algorithm

A. Robust Short-Lag Spatial Coherence (R-SLSC) Imaging

If we define outliers in SLSC images as pixels with coherence values that differ significantly from their surroundings and from their values at other lags, we observe that SLSC images formed with higher lags tend to have more outliers [27]. These outliers adversely affect contrast, and thus reduce the diagnostic utility of SLSC imaging. Consequently, we hypothesize that filtering out these coherence outliers is an important step in order to consider the additional information that is provided at higher lag values.

We also hypothesize that because each image corresponds to an observation of the same ground truth, we can treat the images at the different lags as noisy, corrupted versions of this ground truth, each affected differently by clutter and coherence outliers. We can thus reformulate finding the optimal summation of the coherence images as a RPCA application[26], [28], [29] and we call this combination R-SLSC.

The first step of R-SLSC is to perform SLSC beamforming and generate the coherence images at various lags. Each of these lag images is then vectorized as illustrated in Fig. 1a. The vectorized lag images (up to a specific lag M) are stacked horizontally to form the noisy data matrix D. This matrix D is then fed into the RPCA algorithm, which returns a low rank estimate that corresponds to A in Eq. (7), which is the denoised data matrix, with both coherence outliers (stored in E) and low magnitude dense noise (stored in N) removed. We then apply a weighted sum across the columns to generate the vectorized output R-SLSC image corresponding to lag M. The

weighting applied could be uniform (as in traditional SLSC imaging), but we apply a linearly decreasing weighting scheme (weight 1 to lag image 1, weight $\frac{M-1}{M}$ to lag image 2, ..., weight $\frac{1}{M}$ to lag image M) to enforce our prior knowledge that SLSC image characteristics such as Contrast, CNR, SNR are superior in the short-lag region. We call this weighting scheme linear M-weighting. With linear M-weighting, the higher lag value observations are primarily used to refine our estimate of the data subspace for A in Eq. (7). The final step involves reshaping the vectorized image to obtain the output R-SLSC image corresponding to lag M.

We additionally note that we can vary the λ parameter (see Eqn. 7) to apply a penalty factor to the quantity of coherence outliers present. The λ value reported throughout this paper is multiplied by $\frac{1}{\sqrt{size(D,1)}}$, where D is the data matrix being considered. We chose λ to equal 1 unless otherwise stated.

B. Columnwise and Patchwise R-SLSC Imaging

With the addition of RPCA to SLSC imaging, one expected concern with R-SLSC imaging is the additional processing time. While real-time SLSC imaging has previously been demonstrated [34], [35], performing real-time R-SLSC on the entire image is not possible as currently implemented.

The bottleneck in R-SLSC processing times is the Singular Value Decomposition (SVD) step of the RPCA algorithm. The time complexity, O, of SVD is generally $O(min(mn^2, m^2n))$, where m is the number of rows of the data matrix D and n is the number of columns[42]. Thus, we hypothesize that subdividing the large SVD problem into smaller SVDs, each solved independently using parallel computing, will increase algorithm speed.

We experimented with two methods for subdividing our problem:

- Columnwise R-SLSC (summarized in Fig. 1b)
- Patchwise R-SLSC

To implement columnwise R-SLSC, the first step entails performing SLSC beamforming and generating the coherence images at the various lags. However, instead of vectorizing the images, we extract a specific column from each of these lag images (up to a specific lag M) and stack these extracted columns horizontally to form the noisy data matrix D as illustrated in Fig. 1b. We repeat this process across all columns to achieve n independent RPCA subproblems (where n is the number of columns). The RPCA subproblems are then solved, and the results from each are combined to obtain the final columnwise R-SLSC image corresponding to lag M.

The process for patchwise R-SLSC is similar, with the exception that the independent subproblems correspond to patches and not columns.

IV. Evaluation Methods

A. Simulation Data

Field II[36][37] was used to generate a numerical phantom of width 50 mm, height 60 mm (located between 30 mm and 90 mm depth) and transverse width 10 mm. A total of 3,141,360 scatterers (corresponding to 20 scatterers per resolution cell) were randomly placed in this volume, with amplitudes that were randomly drawn from a standard normal distribution. An anechoic cyst of diameter 4 mm was centered at a depth of 60mm. Focused transmits with dynamic receive were used to image the cyst. The parameters of the simulated probe matched those of the Alpinion L3-8 linear array transducer which was used to acquire experimental data (see Table I for transducer and image acquisition parameters). The sampling frequency was 40 MHz, and the center frequency was 8.0 MHz. Additive white Gaussian noise of SNR -10 dB was added to the channel data and the summed signal was bandpass filtered with cutoff frequencies equal to the -6 dB cutoff frequencies of the ultrasound transducer in order to simulate acoustic noise received by the transducer[11], [33].

TABLE I: Ultrasound Transducer and Image Acquisition Parameters

	Experiments	PICMUS
Aperture Width	19.2 mm	38.4 mm
Element Width	0.24 mm	0.27 mm
Number of Receive Elements	64	128
Pitch	0.30 mm	0.30 mm
Transmit Frequency	8 MHz	5.208 MHz
Sampling Frequency	40 MHz	20.832 MHz
Pulse Bandwidth	61%	67%

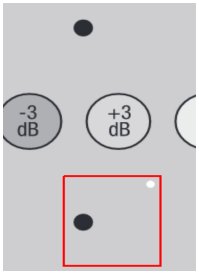

Fig. 2: Schematic diagram of phantom used for the plane wave data. The red rectangle shows the anechoic target of interest for our study.

B. Experimental Phantom and In Vivo Data

Ultrasound data was acquired with an Alpinion E-Cube 12R connected to an L3-8 linear ultrasound transducer. An 8mm diameter cylindrical anechoic cyst target of a CIRS Model 054GS ultrasound phantom at a depth of 4cm was insonified. The sampling frequency of the probe was 40 MHz and the center frequency for the transmission was 8.0 MHz. The probe possessed 128 elements, with only 64 allowed to receive simultaneously at any point in time. Additional transducer and image acquisition parameters are listed in Table I.

Using the same ultrasound system, a 4mm diameter vessel located at a depth of 34mm in the liver of a healthy female was imaged with approval from the Johns Hopkins University Institutional Review Board (Protocol HIRB00005688). The patchwise and columnwise R-SLSC methods were only applied to this *in vivo* dataset. CPU parallelization was performed using the *parfor* subroutine in MATLAB on an Intel(R) Core(TM)

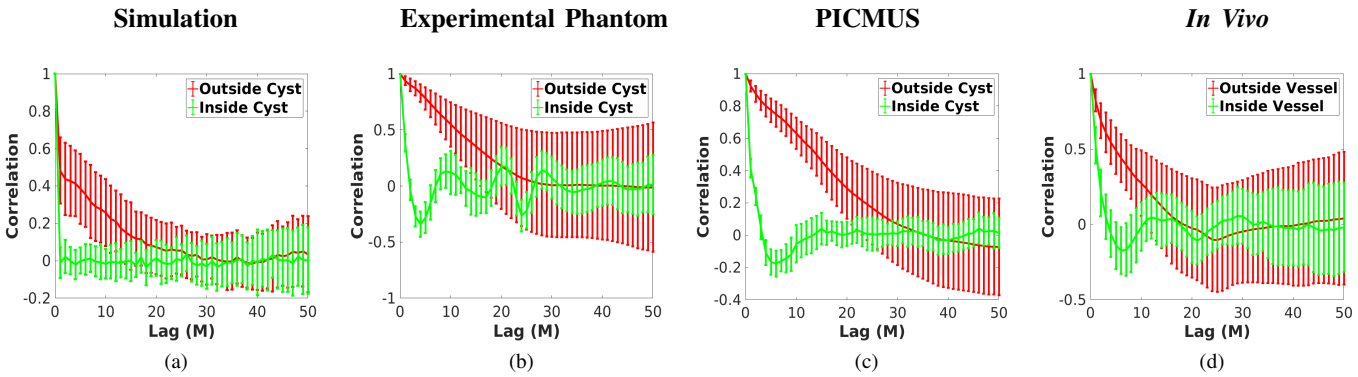

Fig. 3: Measured spatial coherence within regions of interest (ROIs) inside and outside anechoic or hypoechoic targets. The lines show the means and the error bars show ± one standard deviation of the measured spatial correlation within each ROI. The locations of the ROIs relative the cyst are shown in Figs. 4, 6, and 7 for the simulated, phantom, and PICMUS data, respectively.

i7-4720HQ CPU with a clock speed of 2.60 GHz. This *in vivo* dataset was additionally used to experiment with the direct display of M-weighted SLSC images without applying RPCA and to experiment with the optimal λ parameter for R-SLSC imaging.

C. Plane Wave Data

In addition to simulation and experimental data acquired with focused transmits, we tested our algorithm on the publicly available plane wave experimental data provided through the Plane-Wave Imaging Challenge in Medical Ultrasound (PICMUS)[43], which was organized for the 2016 IEEE International Ultrasonics Symposium. The data consisted of 75 steered plane wave sequences with an angular range of -16 degrees to +16 degrees, acquired with a Verasonics Vantage 256 research scanner and a L11 probe (Verasonics Inc., Redmond WA). The probe specifications and acquisition parameters are reported in Table I.

A CIRS Multi-Purpose Ultrasound Phantom (Model 040GSE) was imaged using this setup. Specifically, the region corresponding to a -3dB and a +3dB cyst set against a speckle background with a pair of anechoic targets was recorded. Both cysts are located at a depth of 3cm and have diameters of 8 mm, while the anechoic targets are located at depths of 15mm and 45mm, and are smaller with a diameter of 3mm. The anechoic target located at 45mm depth was the focus of our study, as highlighted by the red box in Fig. 2.

D. Image Quality Metrics

The contrast, signal-to-noise ratio (SNR) and contrast-to-noise ratio (CNR) metrics were calculated for each data set, as:

$$Contrast = 20\log_{10}\left(\frac{S_i}{S_o}\right) \tag{8}$$

with S_i and S_o representing the mean signal intensities inside and outside selected regions of interest (ROIs) at the same image depth.

$$SNR = \frac{S_o}{\sigma_o} \tag{9}$$

where σ_o is the standard deviation of the background ROI.

$$CNR = \frac{|S_i - S_o|}{\sqrt{\sigma_i^2 + \sigma_o^2}} \tag{10}$$

where σ_i is the standard deviation of the signal in the chosen ROI.

Note that SLSC images can contain negative pixels due to potential negative correlations from signals that are out of phase. However, we observed that these negative values mostly appear in anechoic or hypoechoic regions, and they are not significant (i.e., they are closer to 0 than -1). When log compressing an image with negative values, the negative correlations are converted to positive values that degrade the image quality. Hence, our approach when calculating our quality metrics and displaying our images was to set all negative SLSC image pixels to zero.

To evaluate the PICMUS data and to enable past and future users of the PICMUS dataset to compare their results with our method, we additionally report a modified version of the contrast evaluation script provided by the PICMUS challenge organizers. The modified script calculates contrast as:

$$PICMUS\ Contrast = 20\log_{10}\left(\frac{|S_i - S_o|}{\sqrt{\frac{\sigma_i^2+\sigma_o^2}{2}}}\right) \tag{11}$$

All data analysis and beamforming was performed in MATLAB (MathWorks Inc., Natick, MA).

V. Results

A. Correlation Curves

The VCZ theorem predicts that when imaging diffuse scatterers like tissue, the expected spatial correlation across the receive aperture is a triangle, with a peak of 1 at lag 0 and a minimum of 0 at lag $N-1$, where N is the total number of elements in the transmit aperture. However, when imaging anechoic or hypoechoic regions (like the cyst or the vessel), the spatial correlation is expected to significantly drop from 1 to 0 in the short-lag region, with low magnitude oscillations about 0 as lag increases beyond the initial drop [7].

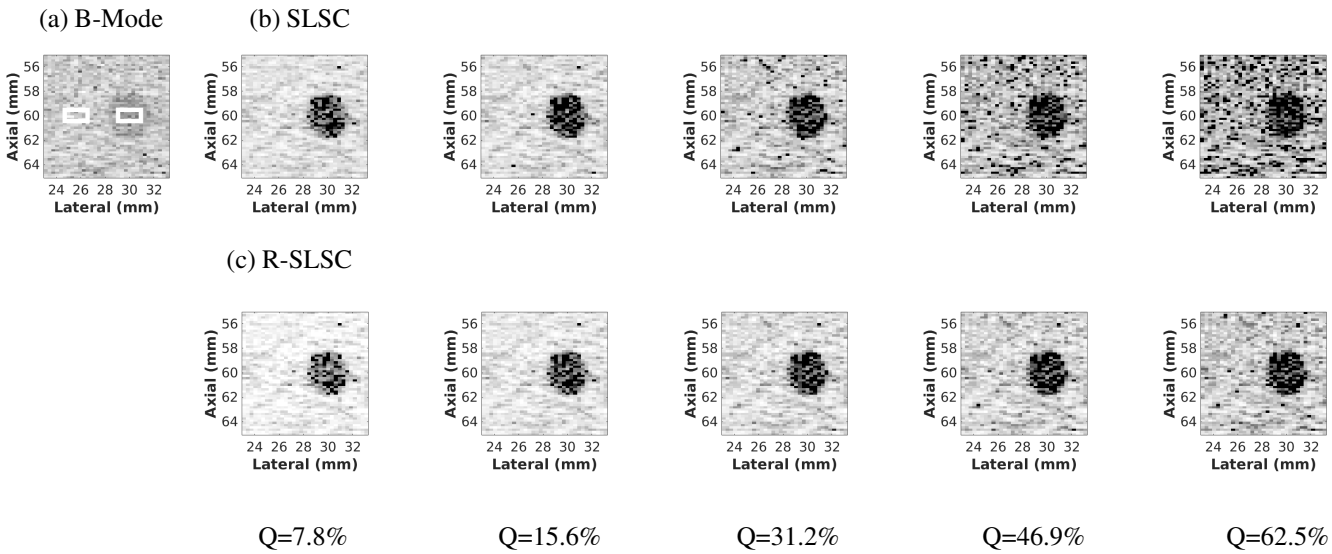

Fig. 4: (a) DAS B-mode image of an anechoic cyst simulated with Field II[36], [37]. The white rectangles show the ROIs used to calculate Contrast, SNR, CNR, and the correlation curves in Fig. 3a. (b) SLSC images corresponding to Q-values of 7.8%, 15.6%, 31.2%, 46.9% and 62.5%, respectively. (c) Corresponding R-SLSC images created with the same Q-values. All images are displayed with 60 dB dynamic range.

We measured the spatial correlation for a pair of rectangular windows (one in the background, and the other within the target), resulting in the correlation curves shown in Fig. 3. The lines correspond to the mean value measured within each ROI, while the errorbars display $\pm$ one standard deviation of the measured correlation within each ROI.

The experimental correlation curves generally agree with our expectations. One notable difference between the simulated and experimental coherence curves is the significant decrease in coherence at lag 1 in simulation, which occurs because of the presence of noise in the simulation[38], [39]. We additionally note that the standard deviations (represented by the amplitude of the error bars) appear to increase as we increase lag both inside and outside anechoic regions. This increase is generally greater outside rather than inside the anechoic region with the exception of the simulation result. Fig. 3 provides evidence that noise and outliers increase as lag increases, which is one primary motivation for pursuing R-SLSC imaging, as we assume that the ground truth for each correlation estimate lies somewhere within the error bars.

B. Simulation Results

B-mode, SLSC, and R-SLSC images of the simulated anechoic cyst target are displayed in Fig. 4. The rectangles in the B-mode image (Fig. 4a) correspond to the regions inside and outside the cyst used to calculate contrast, SNR and CNR, and they were maintained for all performance metrics calculated for this phantom. Fig. 4b shows the SLSC beamformed outputs corresponding to Q-values of 7.8%, 15.6%, 31.2%, 46.9 % and 62.5%, respectively, while Fig. 4c shows the R-SLSC beamformed outputs for the same Q-values. All images are displayed with a 60 dB dynamic range.

The mean gain in R-SLSC contrast (for all Q values considered) is 1.48 dB, when compared to that of SLSC, which corresponds to a mean gain of 4.53%. The mean gains in R-SLSC SNR and CNR (when compared to SLSC SNR and CNR) are 0.35 and 0.35, respectively, which correspond to improvements of 22.72% and 22.87%. The contrast and CNR of SLSC and R-SLSC generally outperform DAS B-Mode in this simulation result, as shown in Fig. 5 (left), particularly at the higher lag values.

C. Experimental Phantom Results

A B-mode image of the anechoic cyst phantom target is displayed in Fig. 6a with white rectangles that demarcate the regions inside and outside the cyst being considered when evaluating contrast, SNR and CNR. The same ROIs are used for all performance metrics calculated with this phantom. SLSC and R-SLSC images of this phantom are displayed in Fig. 6b and 6c, respectively (created with Q-values equal to 7.8%, 15.6%, 31.2%, 46.9 % and 62.5 %).

The mean gain in R-SLSC contrast (for all Q-values considered) is 23.91 dB when compared to that of SLSC, which corresponds to a mean gain of 43.18%. The mean gains in R-SLSC SNR and CNR (when compared to SLSC SNR and CNR) are 2.10 and 2.03, respectively, which correspond to improvements of 65.30% and 63.16%. R-SLSC contrast, CNR, and SNR generally outperform B-Mode imaging for the majority of Q-values considered, as shown in the second column of Fig. 5.

Qualitatively, for this phantom data, we observe that at the lower lags, boundary delineation for R-SLSC is worse than that of SLSC, likely because R-SLSC does not have sufficient data to estimate a suitable subspace. However, this boundary delineation is improved at higher lags when compared to lower-lag R-SLSC images and when compared to comparable-lag SLSC images. We additionally observe that at lower lags

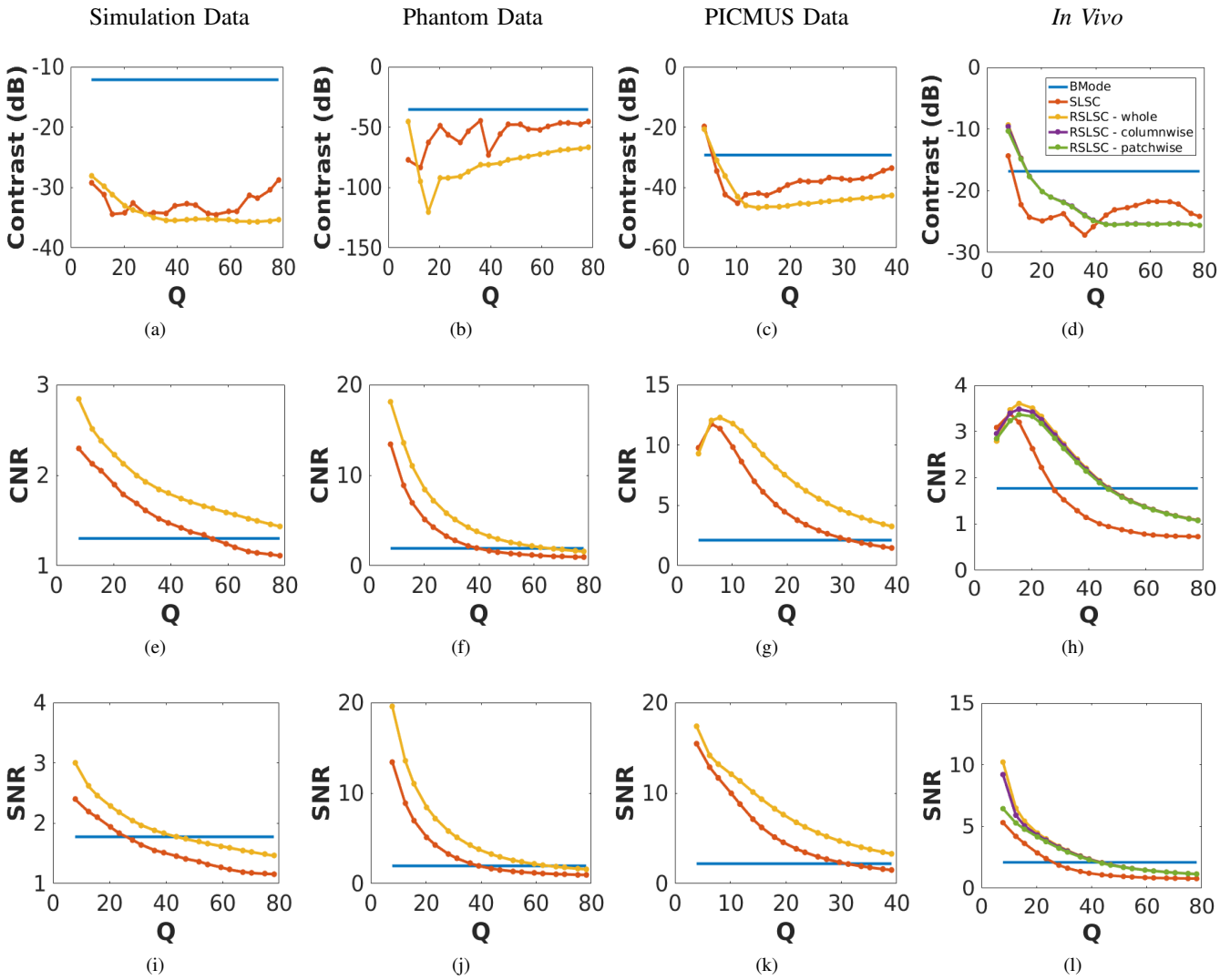

Fig. 5: Comparison of B-mode, SLSC, and R-SLSC Contrast, CNR and SNR measurements and their variation with Q, as measured in (a, e, i) simulated data with -10dB channel noise, (b , f, j) experimental phantom data acquired with focused transmit beams, (c, g, k) experimental phantom data acquired with plane wave transmission, and (d, h, l) *in vivo* liver data. For the *in vivo* liver data, the patchwise and columnwise results overlap the results obtained with R-SLSC applied to the whole image in most cases. B-mode images were created with the entire receive aperture, and the Q values do not apply to the B-mode results.

the poor boundary definition results in seemingly smaller cyst sizes. This is related to the finite width of the ultrasound beam and the lower lags containing only local information, which is insufficient to produce a good boundary estimate. However, at higher lags, the cyst size returns closer to its original size because the algorithm incorporates the higher resolution information that is contained within the higher element separations. The tissue texture surrounding the cyst also appears smoother at the higher-lag R-SLSC images when compared to the higher-lag SLSC images.

D. Application to Plane Wave Imaging

B-mode, SLSC and R-SLSC images of the plane wave data are displayed in Fig. 7. The rectangles in the DAS image (Fig. 7a) correspond to the target and background ROIs used to evaluate contrast, SNR and CNR and they are maintained for this phantom. Fig. 7b shows SLSC images corresponding to Q-values of 7.8%, 15.6%, 23.4%, 31.2% and 39.0%, while Fig. 7c shows corresponding R-SLSC images.

Based on the metrics shown in Fig. 5 for the PICMUS data, R-SLSC has a mean contrast gain (averaged over all Q-values considered) of 4.62 dB (12.28%) when compared to SLSC, with gains in SNR and CNR of 2.37 (42.41%) and 2.14 (41.50%), respectively. Similar to the previous phantom results achieved with focused transmits, R-SLSC imaging outperforms B-Mode imaging for this PICMUS data obtained with plane wave transmits, particularly at higher lags, as evident in Figs. 5c, 5g, and 5k.

We were unable to obtain meaningful results when directly implementing the contrast evaluation script provided by PIC-

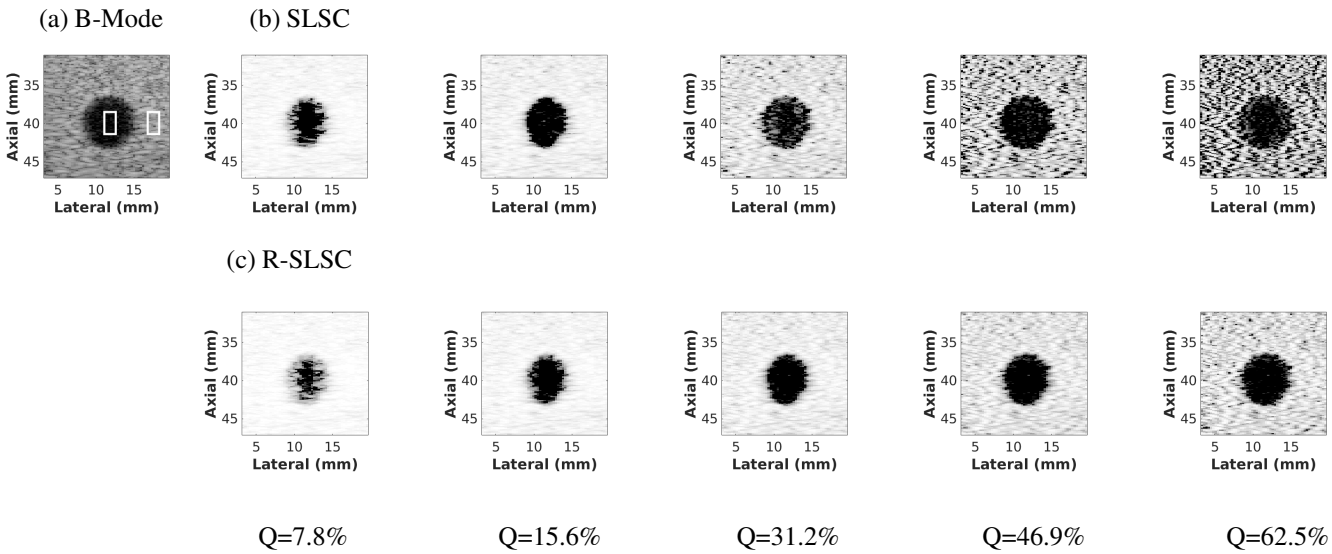

Fig. 6: (a) DAS B-mode image of an anechoic cyst in a CIRS 054GS experimental phantom. The white rectangles show the ROIs used to calculate Contrast, SNR, CNR, and the correlation curves in Fig. 3b. (b) SLSC images corresponding to Q-values of 7.8%, 15.6%, 31.2%, 46.9% and 62.5%, respectively. (c) Corresponding R-SLSC images created with the same Q-values. All images are displayed with 60 dB dynamic range.

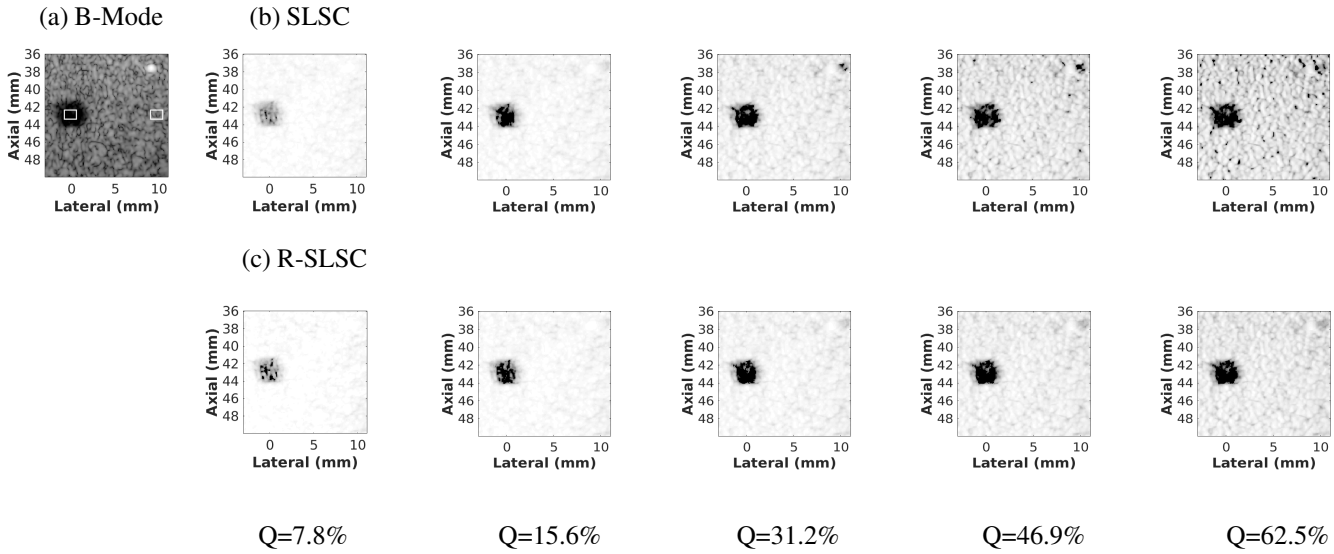

Fig. 7: (a) DAS B-mode image constructed from from the PICMUS[43] experimental data of an anechoic target in a CIRS 040GSE phantom. The white rectangles show the ROIs used to calculate Contrast, SNR, CNR, and the correlation curves in Fig. 3c. (b) SLSC images corresponding to Q-values of 7.8%, 15.6%, 31.2%, 46.9% and 62.5%, respectively. (c) Corresponding R-SLSC images created with the same Q-values. All images are displayed with 60 dB dynamic range.

MUS organizers because the zero-value pixels in R-SLSC images returned $-\infty$ values after applying the log operation step provided in the script. We therefore made one change to the evaluation script and measured performance prior to log compression, resulting in a contrast of 7.90 dB for the DAS B-Mode image and a mean contrast (averaged over all Q-values considered) of 11.95 dB for the R-SLSC images, which confirms our observations that R-SLSC imaging produces better anechoic cyst contrast (4.05 dB greater) than B-mode imaging.

We additionally note that the hyperechoic point target, which is clearly observable in the DAS B-mode image, is difficult to visualize in both the SLSC and R-SLSC images. Generally, SLSC is known to perform poorly with point target visualization [7] (except in the presence of noise[11]). We see that this is also true for R-SLSC imaging with plane wave transmissions. There are also a few coherence outliers within the cyst that are not removed with R-SLSC imaging, although the corresponding location of these outliers have lower amplitudes and are less pronounced in the B-mode

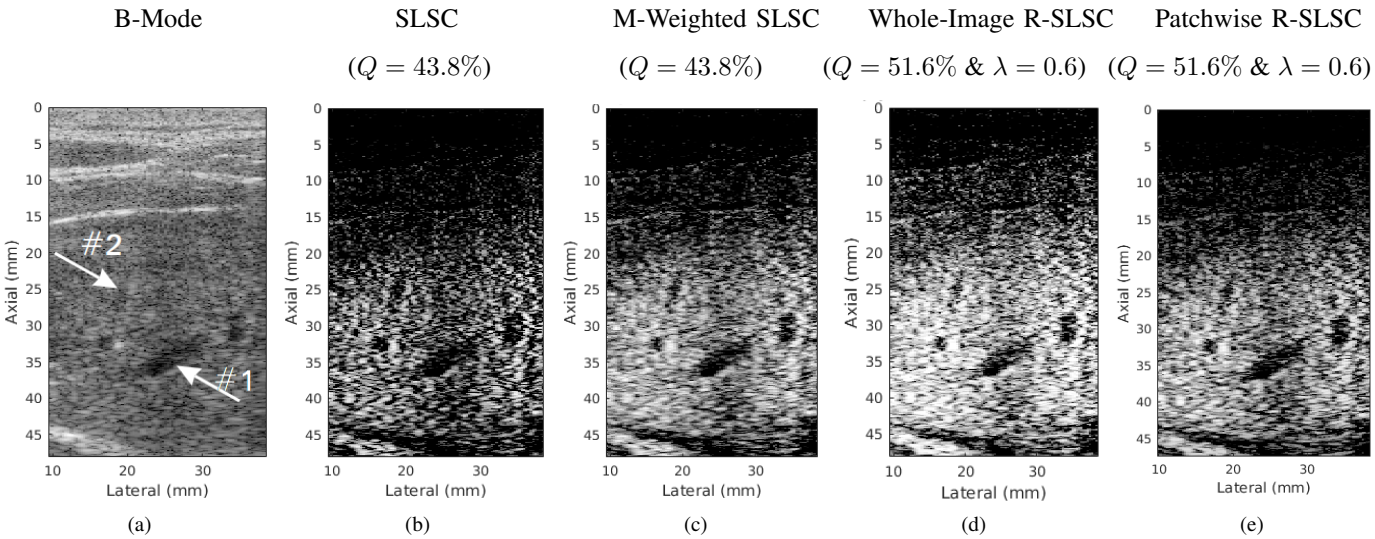

Fig. 8: *In Vivo* images of hypoechoic blood vessels in a healthy liver. (a) B-mode image, (b) traditional SLSC image created with $Q = 43.8\%$, (c) M-weighted SLSC image (without RPCA), (d) whole-image R-SLSC created with $Q = 51.6\%$ and $\lambda = 0.6$, (e) Patchwise R-SLSC image created with $Q = 51.6\%$ and $\lambda = 0.6$. The dynamic range for each image was chosen to best visualize the data (i.e, 60 dB for the B-mode image and 30 dB for the SLSC, M-weighted SLSC, and R-SLSC images). Arrow #1 points to the ROI used to calculate contrast, CNR, and SNR, while arrow #2 points to a vessel that is noticeably improved with SLSC, M-weighting, and R-SLSC.

image.

E. In Vivo Liver Data

B-mode, SLSC, and R-SLSC images of a hypoechoic vessel target in an *in vivo* liver are shown in Figs. 8a, 8b, and 8d, respectively. Although rectangles corresponding to the ROIs used to evaluate contrast, SNR and CNR were omitted to improve vessel visibility, they correspond to the largest vessel at a the transmit focal depth of 35mm, located between lateral positions 20 and 30mm (see arrow #1). We also note that the top of these *in vivo* SLSC and R-SLSC images are dark because they are outside of the focal zone.

The mean R-SLSC contrast loss (averaged over all Q-values shown in the last column of Fig. 5) is 0.48 dB when compared to that of SLSC, which corresponds to a 2% decrease. When we exclude the lower lags from this comparison and only consider the higher lags ranging from $Q = 43.75\%$ to $Q = 78.12\%$ (where we see the most contrast improvement), we achieve a higher mean contrast gain of 2.69dB (11.86%) for R-SLSC images compared to SLSC images. The mean SNR and CNR gains (averaged over all Q values) are 1.26 and 0.67, respectively, corresponding to improvements of 71.62% and 45.26%. Similar to phantom data, R-SLSC imaging outperforms B-Mode imaging for this *in vivo* case, as shown in Figs. 5d, 5h, and 5l. The additional lines seen in this last column of Fig. 5 are explained in Section V-F.

Qualitatively, there are several additional aspects of these R-SLSC *in vivo* images that are improved over SLSC and B-mode images. For example, clutter obscures the appearance of the vessel located from depth 20 mm to 30 mm in the B-mode image (see arrow #2), but this vessel is more clearly visualized in the SLSC and R-SLSC images. The tissue within the transmit focal zone is additionally brighter overall in R-SLSC images (when compared to SLSC images created with similar lag values). Similar to the phantom and simulated data, the tissue texture also appears to be smoother with R-SLSC images. This smoothing of tissue texture helps with discerning the hypoechoic vessels from their surroundings and reduces the speckle-like texture of the images.

F. Parallelization

After calculating delays and computing a SLSC image, the average additional computation time required to calculate the robust principal components is 23 seconds per R-SLSC image (using the computer described in Section IV-B). One approach to reduce the R-SLSC image computation time is to subdivide the RPCA computation for parallel processing as illustrated in Fig. 1b. We successfully implemented this alternative using the same number of columns as scanlines (i.e., 128 columns) for the columnwise implementation and using 64 pixel x 64 pixel patches (i.e. 88 patches total each of size 19.2mm (lateral) $\times$ 1.23mm (axial)) for the patchwise implementation, thereby reducing our RPCA computation times to 9s each. For comparison, Fig. 9 shows the calculation times for these various R-SLSC implementations alongside the calculation times for SLSC correlation calculations and B-mode imaging obtained with the computer described in Section IV-B.

A patchwise R-SLSC image of the *in vivo* liver is shown in Fig. 8e. When comparing the process for creating this image with that of the corresponding R-SLSC image obtained

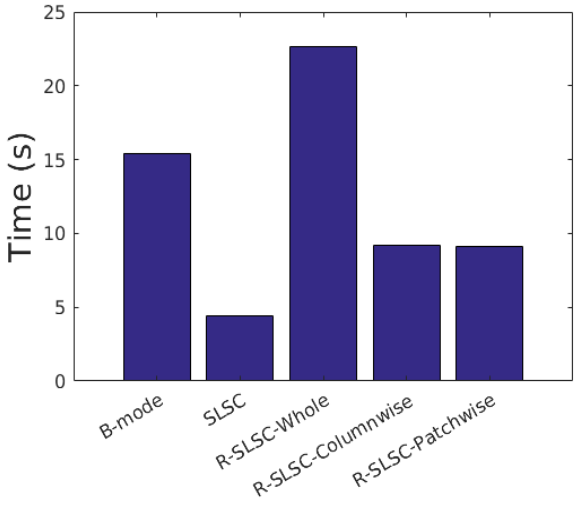

Fig. 9: Calculation times to obtain B-mode and SLSC images with the computer described in Section IV-B, compared to calculation times for the RPCA step required to obtain R-SLSC images with and without patchwise and columnwise parallelization. The calculation time for R-SLSC is reduced by a factor of 2.6 with parallelization.

without parallelization (Fig. 8d), we note that this patchwise image excludes the black region at the top of the image when imaging the vessels closer to the image focus. This exclusion results in slightly less clutter inside vessel # 1 which is close to the focus, although the performance metrics in Fig. 5 are not affected. In addition, the patchwise image slightly reduces the overall image brightness (when compared to the R-SLSC image without parallelization) because this image is based on the local estimates within each patch. Otherwise, the reduction in computation times achieved with parallelization has minimal impact on image quality. This observation is particularly true at the higher lags, which can be confirmed quantitatively by noting that the two additional lines in Figs. 5d, 5h, and 5l (representing the columnwise and patchwise implementations) overlap the whole-image R-SLSC implementation at the higher lags.

G. Effect of the λ Parameter and M-Weighting

As speckle SNR is an important characteristic of ultrasound images, the $Q-$values of the *in vivo* R-SLSC images in Fig. 8 were chosen to closely match the speckle SNR of DAS images. Our specific selections are represented by the open circles in Fig. 10a, which shows the results of our investigations to determine the optimal λ parameter for R-SLSC imaging. While the SLSC images possess high SNR (in most cases higher than B-mode), we find that we can control the SNR more directly in R-SLSC imaging by adjusting the λ parameter.

Fig. 10 shows contrast, CNR, and SNR for B-mode, traditional SLSC, and R-SLSC with λ equal to $1.0, 0.8, 0.6$ and 0.4. We observe from Fig. 10 that decreasing the λ parameter results in applying less penalty to labeling pixels as outliers, and as a result more coherence values are labeled as outliers to be discarded (which effectively increases the SNR). These changes in SNR generally have minimal impact on image contrast, except when λ=0.4 (see Fig. 10b).

When comparing R-SLSC ($\lambda = 1$) to SLSC images created with the linear M-weighting described in Section III-A (applied without RPCA), we observe that the majority of the improvements obtained with R-SLSC are primarily due to this weighting step. For example, an M-weighted SLSC image without the application of RPCA is shown in Fig. 8c, and it looks strikingly similar to the R-SLSC image achieved with the same $Q-$value (43.8%) and $\lambda = 1$, which is confirmed quantitatively in Fig. 10b, as M-weighted SLSC images obtained with different Q-values have similar contrast to R-SLSC ($\lambda = 1$) images. The SNR and CNR of these two image types are also similar at higher lag values (Figs. 10a and 10c). This observation is true not only for the *in vivo* data, but also for the phantom and simulated data (although images are not shown without RPCA applied for these data). Thus, M-weighting is a major step towards improving SLSC image quality and incorporating the information from higher lags.

Despite this similarity between M-weighted SLSC images and R-SLSC images achieved with $\lambda = 1$ (and the significantly reduced processing time required for M-weighted SLSC compared to R-SLSC imaging), R-SLSC imaging can potentially be considered more advantageous because we can use RPCA to incorporate up to 8% more lags (i.e. 43.8% vs. 51.6%, which corresponds to 10 additional element separations for a 128-element aperture) and achieve similar SNR to B-mode images by decreasing the λ parameter, as shown quantitatively in Fig. 10 with an example image displayed in Fig. 8d. Although the number of coherence outliers are greater at higher lags, it appears that more of them are rejected with lower values of λ. This data-dependent adjustment of the λ parameter effectively allows us to utilize more lags, achieve similar speckle SNR to B-mode images, and obtain greater improvements in contrast and CNR when compared to traditional SLSC images achieved with the same Q-values.

VI. Discussion

There are four key contributions of this paper. First, we applied both linear M-weighting and RPCA to the traditional SLSC imaging method in order to incorporate previously discarded information from higher lags. With M-weighting, it appears that the short lags provide more structural information (i.e., general cyst location) while the longer lags provide more boundary information, and both contributions work together to improve image quality for anechoic and hypoechoic targets after incorporating more lags with more weight applied to the short lag region. Additional weighting schemes could be applied in the future to explore the optimal weights for a range of imaging targets and anatomical structures. R-SLSC could be considered as a more advanced weighting scheme that improves image quality by both rejecting coherence outliers and taking advantage of the demonstrated benefits of M-weighting. Our second contribution highlights the data-dependent performance of R-SLSC, which can be tuned to

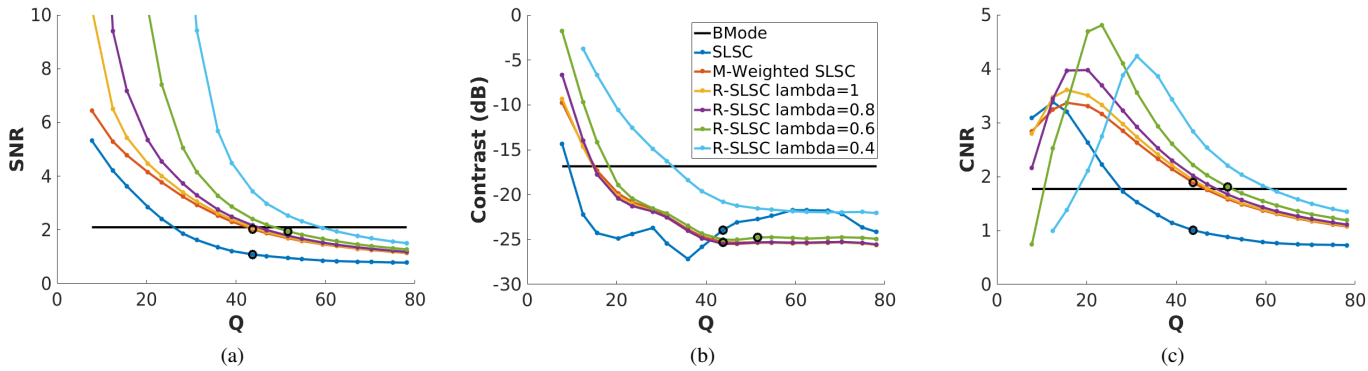

Fig. 10: (a) SNR, (b) Contrast, and (c) CNR of *in vivo* B-mode, SLSC, M-weighted SLSC, and R-SLSC images. The R-SLSC image metrics are calculated with λ = $1.0, 0.8, 0.6$ and 0.4. Note that R-SLSC images can be tuned to provide similar tissue SNR to B-mode images by adjusting the λ parameter, an option that is not possible with SLSC imaging. The black circles correspond to the lags displayed in Fig. 8(b), Fig. 8(c) and Fig. 8(d). B-mode images were created with the entire receive aperture, and the Q values do not apply to the B-mode results.

provide similar tissue SNR to B-mode images by adjusting the λ parameter. Third, we showed that the processing times for R-SLSC can be reduced by subdividing the image data. Finally, we demonstrated that R-SLSC imaging outperforms traditional SLSC imaging (defined as improved SNR, CNR, and contrast of anechoic or hypoechoic regions) at higher lags when applied to data acquired with both focused and plane wave transmissions.

When anechoic and hypoechoic targets are barely discernible in B-mode images due to low contrast and clutter, we expect SLSC and R-SLSC to clearly distinguish these targets from their surroundings, particularly in high-noise environments as represented by the simulation results in Fig. 4 and the *in vivo* results in Fig. 8. R-SLSC experiences additional improvements over SLSC as lag increases in all example cases shown in this paper (simulation, phantom, and *in vivo*), as demonstrated in Fig. 5. This improvement at higher lags is caused by a combination of applying both linear M-weighting and the RPCA algorithm, which develops a better subspace estimate as the amount of data available to the algorithm increases. Therefore, rejection of the noise and outliers is more prevalent at the higher lags, leading to an image with smoother tissue texture. This smoothing of tissue texture helps to discern anechoic and hypoechoic structures from their surroundings and reduces the speckle-like texture of the images, which is generally beneficial for boundary detection (e.g., similar to spatial compounding[44][45]), but could potentially limit the diagnostic information typically provided by the presence of speckle. We can potentially recover some of this diagnostic value by adjusting the λ parameter, which we envision being controlled by an additional knob on an ultrasound scanner, similar to existing options like focal depth or time gain compensation that are currently used to enhance ultrasound image quality. These results imply that both R-SLSC and M-weighting will perform well in high-noise clinical scenarios where anechoic or hypoechoic target visualization is critical. Possible clinical applications include breast cyst visualization [40], liver vessel tracking [41], and obese patient imaging.

One common characteristic between SLSC and R-SLSC images is heightened sensitivity to structural boundaries. For example, when low-amplitude signals are surrounded by hyperechoic structures with high-amplitude signals and high spatial coherence, the coherence of the lower amplitude signal is reduced relative to that of the higher amplitude signal. While this characteristic is a major strength when detecting cyst-like structures, it is also a limitation when imaging hyperechoic boundaries next to tissue structures. This observation was evident in *in vivo* cardiac images[9], and it is present at the distal liver boundary in Fig. 8, where this boundary appears to be separated from the rest of the liver tissue in SLSC and R-SLSC images.

While the processing times for R-SLSC could be considered as an additional limitation of R-SLSC imaging, Fig. 9 demonstrates that it is feasible to subdivide the RPCA step to implement parallel processing for real-time imaging. This alteration provides sufficient information to locally estimate a suitable subspace while rejecting appropriate coherence outliers.

When comparing the SLSC contrast curves for simulated and experimental data in Fig. 5 to the corresponding coherence curves inside the cyst (Fig. 3), the shapes of these curves are similar as a function of Q. While changes in the contrast of SLSC images seems to be correlated with changes in the corresponding coherence curves as a function of Q, the contrast of the R-SLSC images is more stable at higher lags as a result of robustness to coherence outliers. This observation further supports the implementation of R-SLSC imaging.

VII. Conclusion

This work is the first to re-examine the lag summation step of the SLSC algorithm and achieve additional robustness to coherence outliers through both weighted summation of individual coherence images (i.e., M-weighting) and the application of RPCA. The original SLSC imaging algorithm does

not consider the content of the images formed at different lags before summing them, and thus does not exploit tissue texture differences in SLSC images created with various short lag values. In addition, the traditional SLSC beamforming method is somewhat restricted to short lag values when considering the widely varying coherence values present at the longer lags. Our methods improve the original SLSC imaging method by incorporating a linearly decaying weighting scheme to achieve M-weighted SLSC images. RPCA is additionally utilized to search for a low dimensional subspace to the coherence images at different lags. The RPCA projections and consequent denoising of the individual images on this low dimensional subspace are then used to achieve R-SLSC images. Both M-weighted SLSC and R-SLSC imaging enable the use of higher lag information, offer increased contrast, SNR and CNR, and are generally more robust to noise (defined as coherence outliers) when compared to traditional SLSC imaging.

REFERENCES

[1] van Cittert, Pieter Hendrik. *Die wahrscheinliche Schwingungsverteilung in einer von einer Lichtquelle direkt oder mittels einer Linse beleuchteten Ebene.* Physica 1.1-6 (1934): 201-210.

[2] Zernike, Frederik. *The concept of degree of coherence and its application to optical problems.* Physica 5.8 (1938): 785-795.

[3] Goodman, Joseph W. *Statistical Optics.* John Wiley & Sons, 2015.

[4] Mallart, Raoul, and Mathias Fink. *The van Cittert-Zernike theorem in pulse echo measurements.* The Journal of the Acoustical Society of America 90.5 (1991): 2718-2727.

[5] Liu, Dong-Lai, and Robert C. Waag. *About the application of the van Cittert-Zernike theorem in ultrasonic imaging.* IEEE transactions on ultrasonics, ferroelectrics, and frequency control 42.4 (1995): 590-601.

[6] Bamber, Jeffrey C., Ronald A. Mucci, and Donald P. Orofino. *Spatial coherence and beamformer gain.* Acoustical Imaging. Springer US, 2002. 43-48.

[7] Lediju, Muyinatu A., et al. *Short-lag spatial coherence of backscattered echoes: Imaging characteristics.* IEEE transactions on ultrasonics, ferroelectrics, and frequency control 108.7 (2011).

[8] Jakovljevic, Marko, et al. *In vivo application of short-lag spatial coherence imaging in human liver.* Ultrasound in medicine & biology 39.3 (2013): 534-542.

[9] Bell, Muyinatu A. Lediju, et al. *Short-lag spatial coherence imaging of cardiac ultrasound data: Initial clinical results.* Ultrasound in medicine & biology 39.10 (2013): 1861-1874.

[10] Kakkad, Vaibhav, et al. *In vivo performance evaluation of short-lag spatial coherence and harmonic spatial coherence imaging in fetal ultrasound.* Ultrasonics Symposium (IUS), 2013 IEEE International. IEEE, 2013.

[11] Bell, Muyinatu A. Lediju, Jeremy J. Dahl, and Gregg E. Trahey. *Resolution and brightness characteristics of short-lag spatial coherence (SLSC) images.* IEEE transactions on ultrasonics, ferroelectrics, and frequency control 62.7 (2015): 1265-1276.

[12] Hyun, Dongwoon, et al. *Short-lag spatial coherence imaging on matrix arrays, Part 1: Beamforming methods and simulation studies.* IEEE transactions on ultrasonics, ferroelectrics, and frequency control 61.7 (2014): 1101-1112.

[13] Jakovljevic, Marko, et al. *Short-lag spatial coherence imaging on matrix arrays, Part II: Phantom and in-vivo experiments.* IEEE transactions on ultrasonics, ferroelectrics, and frequency control 61.7 (2014): 1113-1122.

[14] Bell, Muyinatu A. Lediju, et al. *Short-lag spatial coherence beamforming of photoacoustic images for enhanced visualization of prostate brachytherapy seeds.* Biomedical optics express 4.10 (2013): 1964-1977.

[15] Bell, Muyinatu A. Lediju, et al. *Improved contrast in laser-diode-based photoacoustic images with short-lag spatial coherence beamforming.* Ultrasonics Symposium (IUS), 2014 IEEE International. IEEE, 2014.

[16] Gandhi, Neeraj, et al. *Photoacoustic-based approach to surgical guidance performed with and without a da Vinci robot.* Journal of Biomedical Optics 22.12 (2017): 121606.

[17] Alles, Erwin J, et al. *Photoacoustic clutter reduction using short-lag spatial coherence weighted imaging.* Ultrasonics Symposium (IUS), 2014 IEEE International. IEEE, 2014.

[18] Pourebrahimi, Behanz, et al. *Improving the quality of photoacoustic images using the short-lag spatial coherence imaging technique*. SPIE BiOS, 2013.

[19] Jolliffe, Ian T. *Principal Component Analysis and Factor Analysis.* Principal component analysis. Springer New York, 1986. 115-128.

[20] Han, Jiawei, Jian Pei, and Micheline Kamber. *Data mining: concepts and techniques.* Elsevier, 2011.

[21] Turk, Matthew, and Alex Pentland. *Eigenfaces for recognition.* Journal of cognitive neuroscience 3.1 (1991): 71-86.

[22] Moore, Bruce. *Principal component analysis in linear systems: Controllability, observability, and model reduction.* IEEE transactions on automatic control 26.1 (1981): 17-32.

[23] Bishop, Christopher M. *Pattern recognition and machine learning.* Springer, 2006.

[24] Mauldin, F. William, Francesco Viola, and William F. Walker. *Complex principal components for robust motion estimation.* IEEE transactions on ultrasonics, ferroelectrics, and frequency control 57.11 (2010).

[25] Prytherch, D. R., et al. *On-line classification of arterial stenosis severity using principal component analysis applied to Doppler ultrasound signals.* Clinical physics and physiological measurement 3.3 (1982): 191.

[26] Wright, John, et al. *Robust principal component analysis: Exact recovery of corrupted low-rank matrices via convex optimization.* Advances in neural information processing systems. 2009.

[27] Bell, Muyinatu A. Lediju. *Improved Endocardial Border Definition with Short-lag Spatial Coherence (SLSC) Imaging.* Diss. Duke University, 2012.

[28] Lin, Zhouchen, Minming Chen, and Yi Ma. *The augmented lagrange multiplier method for exact recovery of corrupted low-rank matrices.* arXiv preprint arXiv:1009.5055 (2010).

[29] Lin, Zhouchen, et al. *Fast convex optimization algorithms for exact recovery of a corrupted low-rank matrix.* Computational Advances in Multi-Sensor Adaptive Processing (CAMSAP) 61.6 (2009).

[30] Mauldin, F. William, et al. *Robust principal component analysis and clustering methods for automated classification of tissue response to ARFI excitation.* Ultrasound in medicine & biology 34.2 (2008): 309-325.

[31] Lediju, Muyinatu A., et al. *A motion-based approach to abdominal clutter reduction.* IEEE transactions on ultrasonics, ferroelectrics, and frequency control 56.11 (2009): 2437-2449.

[32] Lin, Zhouchen, et al. *http://perception.csl.illinois.edu/matrix-rank/sample_code.html*.

[33] Dahl, Jeremy J., et al. *Lesion detectability in diagnostic ultrasound with short-lag spatial coherence imaging.* Ultrasonic imaging 33.2 (2011): 119-133.

[34] Hyun, Dongwoon, Gregg E. Trahey, and Jeremy Dahl. *A GPU-based real-time spatial coherence imaging system.* SPIE Medical Imaging. International Society for Optics and Photonics, 2013.

[35] Hyun, Dongwoon, Gregg E. Trahey, and Jeremy J. Dahl. *Real-time high-framerate in vivo cardiac SLSC imaging with a GPU-based beamformer.* Ultrasonics Symposium (IUS), 2015 IEEE International. IEEE, 2015.

[36] Jensen, Jrgen Arendt. *Field: A program for simulating ultrasound systems.* 10th NORDICBALTIC Conference on Biomedical Imaging, vol. 4, supplement 1, part 1: 351–353. 1996.

[37] Jensen, Jrgen Arendt, and Niels Bruun Svendsen. *Calculation of pressure fields from arbitrarily shaped, apodized, and excited ultrasound transducers.* IEEE transactions on ultrasonics, ferroelectrics, and frequency control 39.2 (1992): 262-267.

[38] Pinton, Gianmarco F., Gregg E. Trahey, and Jeremy J. Dahl. *Spatial coherence in human tissue: Implications for imaging and measurement.* IEEE transactions on ultrasonics, ferroelectrics, and frequency control 61.12 (2014): 1976-1987.

[39] Bottenus, Nick B., and Gregg E. Trahey. "Equivalence of time and aperture domain additive noise in ultrasound coherence." The Journal of the Acoustical Society of America 137.1 (2015): 132-138.

[40] Stavros, A. Thomas. *Breast ultrasound.* Lippincott Williams & Wilkins, 2004.

[41] De Luca, V., et al. *The 2014 liver ultrasound tracking benchmark.* Physics in medicine and biology 60.14 (2015): 5571.

[42] Holmes, Michael, Alexander Gray, and Charles Isbell. *Fast SVD for large-scale matrices.* Workshop on Efficient Machine Learning at NIPS. Vol. 58. 2007.

[43] Liebgott, Herve, et al. *Plane-wave imaging challenge in medical ultrasound.* Ultrasonics Symposium (IUS), 2016 IEEE International. IEEE, 2016.

[44] Trahey, Gregg E., S. W. Smith, and O. T. Von Ramm. *Speckle pattern correlation with lateral aperture translation: Experimental results and implications for spatial compounding.* IEEE transactions on ultrasonics, ferroelectrics, and frequency control 33.3 (1986): 257-264.

[45] Entrekin, R., et al. *Real time spatial compound imaging in breast ultrasound: technology and early clinical experience.* medicamundi 43.3 (1999): 35-43.